Peritectic solidification of Cu–Sn alloys: Microstructural competition at low speed

F. Kohler [a], L. Germond [a], J.-D. Wagnière [a], M. Rappaz [a,*]

[a] *Computational Materials Laboratory, Ecole Polytechnique Fédérale de Lausanne, Station 12, CH-1015 Lausanne, Switzerland*

Abstract

Directional solidification experiments on Cu–Sn peritectic alloys have been conducted at very low velocity in a high-thermal-gradient Bridgman furnace. The size of the samples has been reduced in order to decrease natural convection and the associated macrosegregation. At the lowest growth rates (0.5 and 0.58 µm s^{-1}), eutectic-like $\alpha + \beta$ lamellar structures have been observed in near-peritectic composition alloys over several millimeters of growth. These structures resulted from a destabilization of a band structure in which α- and β-phases overlay each other. Electron backscattered diffraction measurements revealed that bands and lamellae of a solid phase are continuous and originate from a single nucleus.

© 2008 Acta Materialia Inc. Published by Elsevier Ltd. All rights reserved.

Keywords: Directional solidification; Peritectic solidification; Copper alloys; Nucleation and growth; Cooperative growth

1. Introduction

Many commercially important alloys exhibit peritectic transitions during solidification [1], Fe–C, Fe–Ni, Cu–Zn, Cu–Sn and Ti–Al being the most widely known. In such systems, a primary solid α-phase reacts with the liquid phase to form a peritectic β-phase at the peritectic temperature T_p.[1] Indeed, at T_p, the α, β and liquid phases are in equilibrium and the peritectic composition range can be separated into two regions: the hypoperitectic region from C_α to C_p and the hyperperitectic region from C_p to C_L, where C_α, C_p and C_L correspond to the equilibrium compositions of the primary α-phase, of the peritectic β-phase and of the liquid phase at T_p, respectively (see Fig. 1).

In the hypoperitectic region of peritectic metallic systems, various new microstructures have been revealed during directional solidification experiments at low growth rates, i.e. under conditions where both α- and β-phases would grow independently as planar fronts [2]: (i) discrete bands of α- and β-phases; (ii) partial bands or islands of one phase in the matrix of the other phase; and (iii) simultaneous growth of both phases with a planar solid–liquid interface.

Discrete bands and islands have been observed in several peritectic systems, including Fe–Ni alloys [1,3–11], and their formation has been attributed to a succession of nucleation events followed by the growth of one phase (α or β) ahead of a growing planar front of the other phase (β or α). As will be revisited in Section 2, this alternance of α- and β-layers (or partial layers) is due to the fact that neither planar front is stable. For peritectic alloys, Hunziker et al. [12] developed the nucleation and constitutional undercooling criterion (i.e. the NCU model): under the assumption of infinitely high nuclei density and steady-state growth, they established a microstructure map based on the nucleation undercooling of each phase. In highly convective hyperperitectic alloys, tree-like structures appeared during preliminary observations as alternate bands and islands in longitudinal cross-sections. However,

---

[1] For ease of notation, α and β will refer to the primary phase and the peritectic phase throughout this paper, respectively.
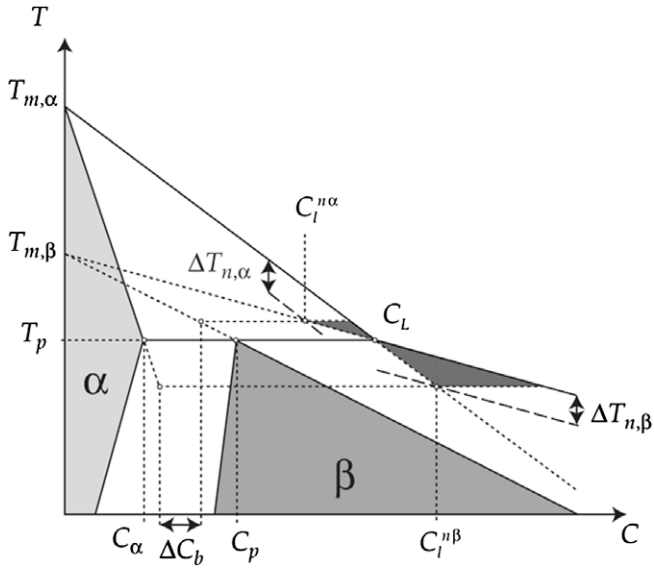
Fig. 1. Schematic illustration of the banding mechanism developed by Trivedi for initial alloy compositions situated in the banding window ΔC_b, for k_α and $k_\beta < 1$ [4]. $\Delta T_{n,\alpha}$ and $\Delta T_{n,\beta}$ correspond to the nucleation undercoolings for the α- and β-phases, respectively.

extensive analyses in Pb–Bi and Sn–Cd alloys [13,14] revealed that these structures are in fact continuous and result from an oscillatory movement of the triple junction due to convection in the melt.

Simultaneous growth of the primary and peritectic phases in the form of oriented lamellae or fibers has rarely been observed. In 1959, Chalmers [15] predicted that a coupled growth similar to that observed in eutectic alloys should be possible for compositions in the two-solid phase region of peritectic systems. A few years later, Livingston [16] and Flemings [17] supported this prediction and argued that a high thermal gradient is also necessary to suppress morphological instability of both phases and allow coupled growth. In 1974, Boettinger [3] performed directional solidification experiments on Sn–Cd alloys, but did not find eutectic-like coupled growth. Nevertheless, he applied the Jackson–Hunt model, formerly developed for lamellar growth in eutectic alloys, to see whether coupled growth was theoretically possible. Based on Cahn's stability arguments, Boettinger concluded that coupled growth of the primary and peritectic phases was unlikely. Only many years later, Lee and Verhoeven [18] carried out directional solidification experiments on Ni–Al alloys and observed the formation of lamellar growth. Furthermore, they demonstrated that the apparently coupled solid–liquid interface was isothermal and slightly below the peritectic temperature. More recently, Vandyoussefi et al. [19] and Dobler et al. [11] have done extensive solidification experiments on Fe–Ni alloys for nominal composition $C_\alpha < C_0 < C_p$. Depending on the growth conditions and local composition, a eutectic-like lamellar structure was observed. Metallographic analyses led to the conclusion in this case that the lamellar growth front was isothermal and slightly above the peritectic temperature.

Despite these recent studies, peritectic solidification at low growth rate is not fully understood. Additionally, eutectic-like lamellar growth was observed only for peritectic systems, such as Fe–Ni and Ni–Al alloys, for which the solidification interval of the primary phase, ΔT_0^α, is fairly small. In order to see if such microstructures can exist for peritectic alloys with fairly large ΔT_0^α, the peritectic Cu–Sn system has been chosen in the present investigation because of its remarkable properties and technological importance (see Section 3). Directional solidification (DS) experiments on Cu–Sn alloys of various compositions have been conducted at different velocities, using a high-thermal-gradient Bridgman furnace. The set-up already used by Dobler [7] has been modified in order to reduce the size of the samples and, accordingly, natural convection, following the original idea of Trivedi and co-workers [20]. During each solidification run, two different geometries were thus tested, allowing the observation of convection effects on the formation of peritectic microstructures. Extensive analyses, including optical microscopy (OM), scanning electron microscopy (SEM), microprobe and electron backscattered diffraction (EBSD), have been done in order to characterize the solidified microstructures.

2. Theoretical background

Let us briefly recall here the underlying solidification mechanisms responsible for the microstructures found in the *hypoperitectic* region at low growth rates, i.e. for $C_\alpha < C_0 < C_p$ (see Fig. 1). During the initial transient period of α-planar front growth, a solute-enriched boundary layer is built. Accordingly, the temperature of the front decreases from the corresponding liquidus temperature $T_l^\alpha(C_0)$ to the solidus temperature $T_s^\alpha(C_0) = T_l^\alpha(C_0/k_\alpha)$, where k_α is the partition coefficient of the α-phase. As soon as the liquid composition at the α–liquid interface, $C_l^{*\alpha}$, exceeds C_L, it becomes undercooled with respect to the β-phase. Thus, the β-phase can nucleate heterogeneously at temperatures below T_p once its nucleation undercooling $\Delta T_{n,\beta}$ is reached [21–25] (see Figs. 1 and 2). Once the peritectic phase has nucleated, growth competition is initiated between the pre-existing phase and the newly nucleated phase. To a first approximation, Trivedi [4] and Trivedi et al. [8,20] assumed an infinitely fast lateral spreading of the newly nucleated phase. Hence, the β-phase entirely covers the primary phase and prevents it from further growth. Trying to reach its corresponding steady-state value, the composition $C_l^{*\beta}$ at the β–liquid interface has now to decrease toward C_0/k_β, where k_β is the partition coefficient of the β-phase ($k_\beta > k_\alpha$). As soon as $C_l^{*\beta}$ falls below C_L, the liquid becomes now undercooled with respect to the primary phase. When the undercooling reaches a critical value $\Delta T_{n,\alpha}$, the α-phase can nucleate and then cover the β-phase, and this so-called banding cycle can start again (see Fig. 1). Then, assuming a purely diffusive growth regime with a negligible diffusion coefficient in the solid phases, i.e. $D_s = 0$, Trivedi [4] developed an analytical model based
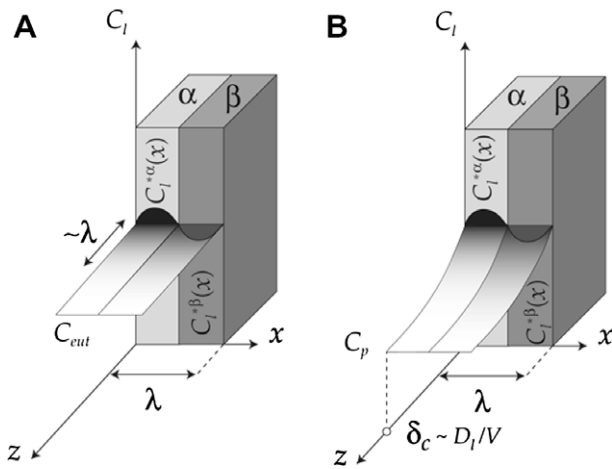
Fig. 2. (A) Isothermal coupled growth for a eutectic alloy of initial composition C_{eut}: at a temperature below the eutectic temperature, the composition of the liquid at the α–liquid interface, $C_l^{*\alpha}$, is higher than C_{eut}, while the composition $C_l^{*\beta}$ at the β–liquid interface is lower than C_{eut}. Therefore, a strong lateral diffusion coupling is established and solute atoms diffuse from the α-phase to the β-phase. (B) Hypothetical isothermal coupled growth for a peritectic alloy of initial composition C_p [7]: above T_p, the composition $C_l^{*\alpha}$ at the α–liquid interface is higher than $C_l^{*\beta}$ at the β–liquid interface. Moreover, a composition profile exists in the liquid phase ahead of both lamellae. In (A) and (B), λ and δ_c correspond to the lamellar spacing and to the diffusion boundary layer, respectively. Redrawn from Dantzig and Rappaz [28].

on the mechanism described above and found the critical concentrations $C_l^{n\beta}$ and $C_l^{n\alpha}$ for band growth (see Fig. 1).

In order to explain the formation of islands rather than bands, the above approximation of infinitely fast lateral spreading of the solid phases must be relaxed. Moreover, the nucleation dynamics must be considered: as analyzed by Trivedi in a recent paper [26], the peritectic phase may nucleate at the α–liquid interface, at the α–liquid–crucible corner or at the liquid–crucible interface. Depending on the nucleation site, various microstructures are expected: for example, if the β-phase nucleates at the α–liquid interface and if the nucleation density is high enough, island growth is favored due to growth competition. Based on geometrical considerations, Trivedi defined a nucleation map for the β-phase: as a function of the contact angles between the α- and β-phases and between the β-phase and the crucible, this map identifies the most probable site for heterogeneous nucleation [26]. Obviously, another map for the heterogeneous nucleation of the α-phase ahead of a growing β-planar front may be defined in the same way. Then, once the β-phase has nucleated, it tends to grow simultaneously in the lateral and in the thermal gradient directions. Accordingly, far away from the triple junctions, both α- and β-phases tend towards their steady-state solidus temperature: the temperature of the α–liquid interface should therefore decrease, while the opposite should occur for the β–liquid interface. When considering the propagation of one solid phase over the other, a mechanical equilibrium condition at the α–β–liquid triple junction must also be considered. The Young–Laplace equation describing this equilibrium is given by:

$$\vec{\tau}_{\alpha l}\sigma_{\alpha l} + \vec{\tau}_{\beta l}\sigma_{\beta l} + \vec{\tau}_{\alpha\beta}\sigma_{\alpha\beta} = 0 \qquad (1)$$

where $\vec{\tau}_{ij}$ corresponds to the unit vector tangential to the i–j interface and pointing outward from the triple junction, while $\sigma_{\alpha l}$, $\sigma_{\beta l}$ and $\sigma_{\alpha\beta}$ are the corresponding surface energies (assumed to be isotropic in this case). The lateral propagation of one solid phase over the other results from a complex interplay between diffusion in the liquid phase and local curvature undercooling near the triple junction [5,8].

Lo et al. [9] conceptually described the transition between bands and islands: based on the consideration of characteristic times necessary for the β-phase lateral propagation and diffusion of solute ahead of the advancing α–liquid interface, a critical distance was found. Contrary to what could be expected, Lo et al. [9] showed that island growth occurs for internuclei distances below this critical distance, while band growth is expected above this distance. Finally, the nucleation of the primary phase may occur on the β–liquid interface far away from the triple junction, thus initiating an additional growth competition. Then, the lateral growth front of the newly nucleated α-phase probably catches the already growing α–liquid interface, thus preventing the β-phase from growing further. Successive rows of islands may form as long as this solidification sequence is followed. Unfortunately, still missing crystallographic orientation measurements do not allow experimental confirmation of the described solidification mechanisms responsible for the transition from bands to islands. Therefore, it is not possible to check if islands correspond to isolated nucleation events or if they result from a complex three-dimensional (3-D) growth morphology.

Lately, directional solidification experiments and multiphase field simulations [7,9–11,27] have shown that islands may be either sustained in time or become seeds for a eutectic-like lamellar structure as long as the distance between islands falls in a range of stable lamellar spacings [9]. Indeed, this structure has been observed experimentally for large volume fractions of the peritectic phase in hypoperitectic Fe–Ni alloys and at G_l/V_p ratios well above the constitutional undercooling criterion of both phases to suppress morphological instability. Dobler [7] and Dobler et al. [10,11] also showed that the transition from islands to lamellae was not spontaneous, but often required a finite distance which could be several millimeters. In several studies, the observed lamellar growth in peritectic alloys is termed "coupled growth", with reference to eutectic growth. However, despite the apparent similarities of microstructures, the diffusion coupling is quite different in eutectic and peritectic coupled growth (see Fig. 2): in eutectic alloys, the solute rejected by one phase is needed by the other phase (see Fig. 2(A)), thus establishing a strong lateral diffusion coupling. In peritectic alloys, since the phase diagram exhibits liquidus slopes of the same sign for the primary and peritectic phases, both solid phases reject solute in the liquid phase. This induces an important solute boundary layer of thickness D_l/V_p ahead of both phases in addition to the diffusion between the phases

(Fig. 2(B)). Although similar to eutectic alloys with off-eutectic initial composition, the coupling between the phases is much weaker in peritectic systems (Fig. 2(B)). Considering that solute diffusion should occur from the α- to the β-phase, i.e. the primary phase rejects more solute than the peritectic phase, Dobler and co-workers [7,10,11] concluded that the α + β lamellar growth front is at a temperature T^* above the peritectic temperature T_p. Indeed, based on metallographic analyses, these authors showed that the apparently coupled lamellar front was isothermal and positioned slightly above T_p, i.e. it was subject to superheating. Interestingly, a probable crystallographic orientation relationship between the α- and β-phases has led to the formation of well-aligned lamellae.

3. Cu–Sn phase diagram

Compared to the Fe–Ni peritectic system, Cu–Sn alloys exhibit a solidification interval of the α-phase, ΔT_0^α, which decreases with an increasing tin composition in the hypo-peritectic composition range. Accordingly, the critical velocity V_c for α-planar front growth increases from $C_0 = C_\alpha$ to $C_0 = C_p$. Additionally, ΔT_0^α is about 25 times larger in the Cu–Sn system than in the Fe–Ni peritectic system. As a consequence, directional solidification experiments must be conducted at very low velocities in order to guarantee morphological stability of both solid phases. But a major advantage originates from this large solidification interval: all contributions are amplified, whether regarding the lateral propagation of a solid phase or the growth of lamellar structures. Therefore, it should be possible to determine more accurately whether the α- and β-lamellae really grow as an isothermal front at a temperature T^* and whether T^* is above or below T_p. However, Cu–Sn alloys also exhibit a few important difficulties. Indeed, strong convective motions are expected in the melt due to a density difference of about 20% between pure copper and pure tin, tin being lighter than copper. Additionally, several solid-state transformations of the β-phase are expected upon cooling (see Section 5).

In the Cu–Sn system, the primary α-phase is a face-centered cubic (fcc) structure. On the other hand, according to Pearson [29], Cortie and Mavrocordatos [30] and Liu et al. [31], the peritectic β-phase is a disordered A2 body-centered cubic (bcc) structure (see Fig. 3). In the literature, numerous Cu–Sn phase diagrams can be found and, most often, these phase diagrams differ slightly. Notably, the reported temperature T_p of the peritectic reaction α + liquid → β varies between 795.7 and 798 °C and the equilibrium concentrations C_α, C_p and C_L are not defined accurately. In a recent publication [32], single pan thermal analyses performed on Cu–Sn alloys revealed that the phase diagram reinvestigated by Liu et al. [31] is the most reliable, even if the peritectic temperature and the corresponding equilibrium concentrations are not assessed accurately.

In the present study, a Cu–Sn phase diagram linearized near the peritectic temperature $T_p = 795.7$ °C has been considered, with $C_\alpha = 13.5$ wt.% Sn, $C_p = 22$ wt.% Sn and $C_L = 25.5$ wt.% Sn (Table 1).

4. Experimental method

Directional solidification experiments have been conducted at different pulling velocities V_p for initial Cu–Sn alloy compositions C_0 close to C_p: $C_0 = 18.7$ wt.% Sn,
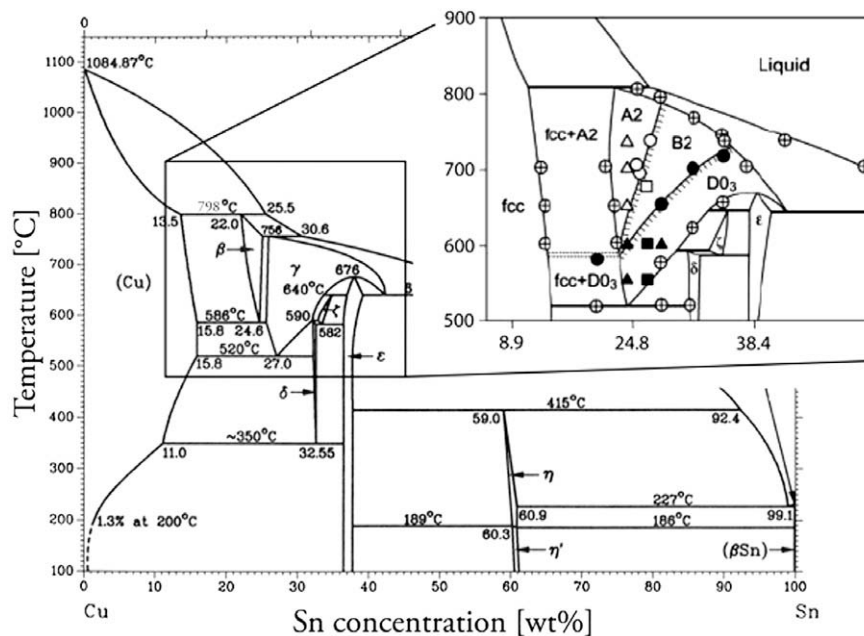

Fig. 3. ASM Cu–Sn phase diagram [33]. An enlargement of the β- and γ-phases regions shows the Cu–Sn phase diagram recently reinvestigated by Liu et al. [31].

Table 1
Parameters of the Cu–Sn phase diagram linearized near the peritectic temperature T_p: for a solid phase ν, $m_{s,\nu}$ and $m_{l,\nu}$ correspond to the slopes of the solidus and liquidus lines, respectively, k_ν is the corresponding partition coefficient

	$m_{s,\nu}$ [K/wt.% Sn]	$m_{l,\nu}$ [K/wt.% Sn]	k_ν
α	−8.08	−11.03	0.53
β	−8.92	−5.53	0.62

Note the smaller slope of the α-solidus due to the particular shape of the phase diagram.

20 wt.% Sn, 21 wt.% Sn, 21.3 wt.% Sn and 23.5 wt.% Sn. All solidification parameters are reported on the corresponding NCU map (see Fig. 4).

The Bridgman furnace that has been used in this work is composed of [7,34]: (i) a closed chamber containing a cylindrical molybdenum susceptor surrounded by an induction coil that controls heating; (ii) a water-cooled Ga–25 wt.% In–13 wt.% Sn liquid metal cooling (LMC) bath for efficient heat extraction and a high thermal gradient; and (iii) an adiabatic zone in-between. In order to reduce natural convection and the associated macrosegregation, a device similar to that introduced by Trivedi et al. [20] was used. As the natural convection intensity is proportional to the cubic power of the characteristic sample size, the volume inside the alumina crucible (inner diameter (ID) 6 mm) was separated into two regions by an alumina capillary (outer diameter (OD) 4 mm, ID 3 mm). Two boron nitride rings allowed to center the capillary inside the alumina crucible (see Fig. 5). In this way, for each experimental run, a Cu–Sn cylinder of 3 mm diameter and a Cu–Sn tube of 4/6 mm ID/OD diameters, i.e. tube of 1 mm in thickness, have been solidified under the same conditions (see Fig. 5).

Fig. 5. Set-up used to solidify Cu–Sn samples. (A) Side view of the set-up, with the dimensions of the alumina capillary and of the BN rings. (B) Illustration of the positioning of the 4/6 mm tube and of the cylinder of 3 mm diameter. The upper ring can slide to maintain a perfect alignment between the capillary and the crucible.

After an initial controlled heating of the susceptor up to 1150 °C, directional remelting of the samples from the upper position was then started on the descent at 1 mm min^{-1} until they were immersed 30 mm in the LMC bath. To establish a high thermal gradient, the susceptor temperature was then further increased to 1500 °C, followed by a thermal arrest of 45 min for thermal stabilization. Following these steps, directional solidification was made at the desired pulling velocity for a processing length of 50 mm, i.e. until the samples were immersed 80 mm in the LMC bath. The Cu–Sn samples were then quenched in the LMC bath. Temperature measurements performed during a DS experiment on a Cu–10 wt.% Sn alloy showed a steady-state temperature profile during solidification, with an average thermal gradient $G_l = 20$ K mm^{-1} determined at the peritectic temperature.

All samples were cast in a vacuum induction furnace from appropriate weights of pure Cu (99.99 wt.%) and pure Sn (99.99 wt.%). Subsequently, wire-electrodischarge machining (EDM) was used to machine the cast samples into tubes and cylinders. Finally, the machined tubes and cylinders were plunged into an etching solution (50 vol.% NH$_3$ and 50 vol.% CH$_3$COOH) for about 5 s and thoroughly cleaned with ethanol in an ultrasonic bath to remove all machining residues and the thin oxide layer formed during wire-EDM.

Once a DS experiment was finished, the samples were cut in three identical 35-mm-long sections. Subsequently, all sections were bisected longitudinally and the alumina capillary was removed. The resulting half cylinder and half tube were then hot mounted together in a conducting resin. In order to observe the peritectic microstructures, the following standard procedure was used: rough polishing was carried out using silicon carbide papers of grades 500, 1000, 1200, 2400 and 4000. Fine polishing was then performed using 1 and 0.25 μm diamond particles on soft cloths. Between each polishing step, the samples were cleaned first with water and soap and then with ethanol in an ultrasonic bath for 2 min. Finally, vibrating polishing
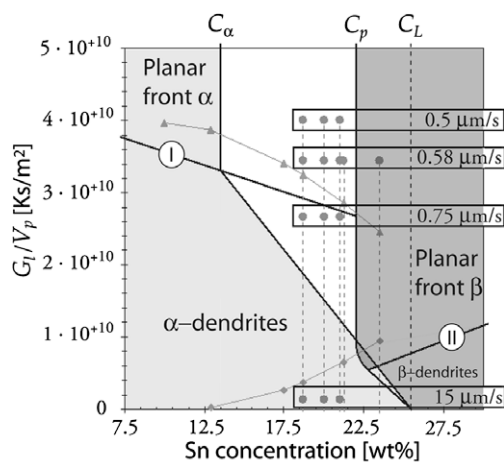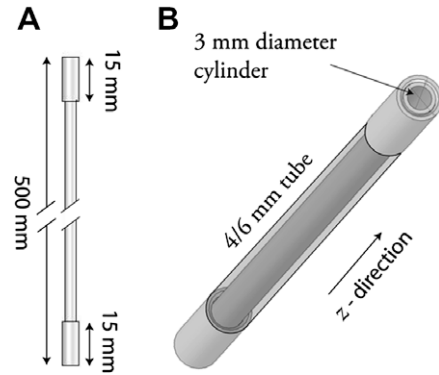

Fig. 4. Representation on a NCU map of the solidification parameters for Cu–Sn alloys, i.e. initial alloy compositions and pulling velocities V_p ($G_l = 20$ K mm^{-1}, $D_l = 4 \cdot 10^{-9}$ m^2/s). C_α, C_p and C_L correspond to the equilibrium compositions at the peritectic temperature. For a simplified linear phase diagram, the lines I and II are the critical G_l/V_p ratios for α- and β-planar front growth, respectively. For a non-linear Cu–Sn phase diagram, the critical ratios are represented by grey curves marked with symbols: triangles for the α-phase and diamonds for the β-phase.

has been carried out for half an hour on a soft cloth using a colloidal suspension. After polishing, rapid chemical etching was done to reveal the phases present in the microstructures. For this purpose, all samples were plunged for 5 s in a solution of potassium chromate $K_2Cr_2O_7$, sulphuric acid H_2SO_4 and distilled water (solution provided by Wieland–Werke AG, [35]). Electron backscattered diffraction (EBSD) analyses require a perfectly planar surface of the sample that is free of deformation. Prior to such analyses, all samples were polished once again according to the standard procedure described above. However, in order to remove the thin work-hardened layer produced during mechanical polishing, an additional vibrating polishing has been carried out for 1 h on a soft cloth using a colloidal suspension in which 2 vol.% NH_4 and 2 vol.% H_2O_2 were added.

5. Results and discussion

The present paper presents the most interesting results obtained at 0.5 and 0.58 μm s^{-1}. Other results can be found in Ref. [34]. At these pulling velocities and with $G_1 = 20$ K mm^{-1}, the α- and β-phases are morphologically stable regardless of the composition if $C_0 > 17$ wt.% Sn (see Fig. 4). This is due to the particular shape of the Cu–Sn phase diagram, which shows a decreasing ΔT_0^α with increasing C_0 (and $\Delta T_0^\alpha > \Delta T_0^\beta$).

An important issue must be addressed here: for all DS experiments, two solid-state phase transformations have been identified for the β-phase: (i) the quench induced a partial decomposition of the β-phase into an acicular martensitic microstructure for compositions between about 22 and 24 wt.% Sn, thus preventing its indexing during EBSD analyses; and (ii) in agreement with single pan thermal analyses made on Cu–Sn alloys [32], the β-phase also transformed to an α + δ lamellar structure via a eutectoid reaction for temperatures below 520 ± 5 °C.

5.1. Band structure

Fig. 6 shows the longitudinal section of a cylindrical sample of a Cu–20 wt.% Sn alloy solidified at 0.5 μm s^{-1}. In Fig. 6(A), the α-phase appears in light brown, whereas darker regions correspond to the β-phase. As can be seen on the temperature scale, the bottom region of the micrograph corresponds to a zone nearly 300 °C below the peritectic temperature. Moving toward the top, the fraction of the β-phase increases, indicating that some macrosegregation is present, i.e. solute enrichment in the liquid phase. Focusing first on the bottom of Fig. 6, it appears that after the initial solute transient associated with the growth of an α-planar front, bands of α- and β-phases form successively (region near the profile P1, see Fig. 6). Fig. 6(B) shows an inverse pole figure based on EBSD measurements of the primary phase only. As can be seen, the α-phase region near the bands is mainly made of two solid grains (appearing purple and blue). However, successive α-lamellae in
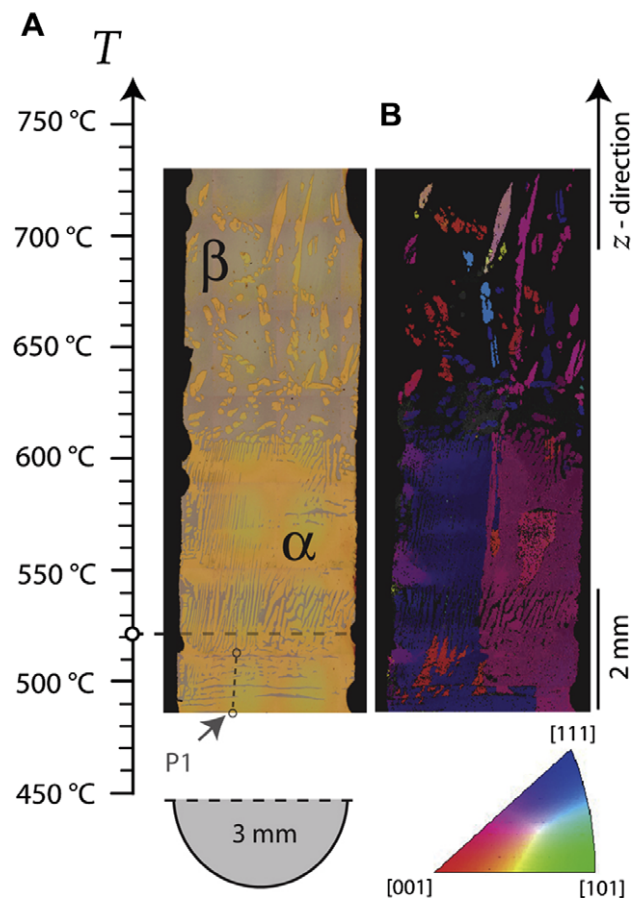

Fig. 6. (A) Solidification sequence in the 3 mm diameter cylinder of a Cu–20 wt.% Sn alloy directionally solidified at 0.5 μm s^{-1} ($G_1 = 20$ K mm^{-1}, α-phase = light brown, β-phase = dark brown). P1 represents the position of the measured composition profile. (B) EBSD analysis in the inverse pole figure representation ([0 0 1] direction parallel to the z-direction).

each grain have the same color and thus the same crystallographic orientation. Although heteroepitaxy can occur between the α- and β-phases, it is much more likely that the α-bands form not by a nucleation mechanism ahead of the β-front, but rather by an overlay mechanism, which is detailed further below.

Local compositions were measured in the solidification direction, i.e. z-direction, using a microprobe as shown in Fig. 7 along the line P1 from Fig. 6. For the sake of clarity and due to the decomposition of the peritectic phase into a eutectoid α + δ lamellar structure, the measured compositions in the formally β-phase region are not shown in Fig. 7.

In each of the α-bands, the composition exhibits a U-shape profile. Close to the α–β interfaces, the composition $C_\alpha^{*\beta}$ in the various α-bands increases from 16.3 wt.% Sn to 16.7 wt.% Sn, then decreases to about 16 wt.% Sn. Since these compositions were measured in the microstructure for positions corresponding to 500 °C at the time of the quench (see Fig. 6(A)), they correspond fairly well to the solvus of the α-phase in equilibrium with the tin-rich δ-phase (or with the β/γ-phase above 520 °C). Indeed, the
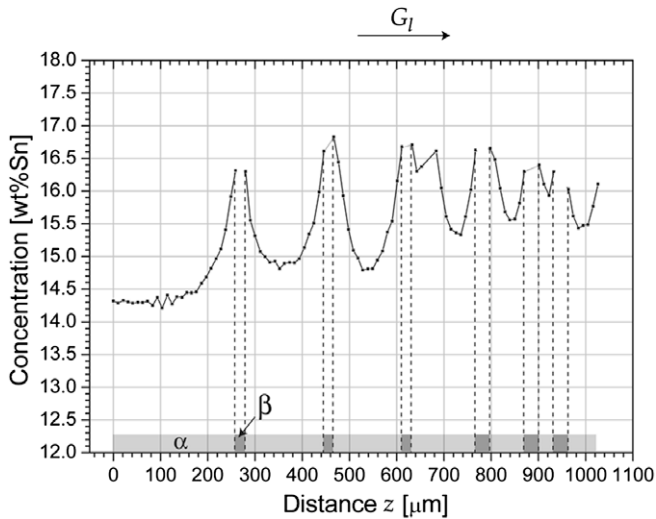
Fig. 7. Local compositions measured along the profile P1 of Fig. 6 in the band structure (3 mm diameter cylinder, Cu–20 wt.% Sn, $V_p = 0.5$ μm s^{-1} and $G_l = 20$ K mm^{-1}).

$$D_s(T) = 1.82 \cdot 10^{-5} \exp\left(-\frac{1.56 \cdot 10^5}{RT}\right) \qquad (2)$$

Then, the Fourier number has been integrated from T_p to 500 °C:

$$F_o = \int_0^{t_d} \frac{4D_s(T(t))}{d^2}\, dt \approx 0.4 \qquad (3)$$

This shows that there is no complete solute mixing in the bands, and the minima of the U-shape composition profiles in Fig. 7 are thus closer to the composition in the α-phase during solidification. In the largest α-band (first band), where diffusion toward the center of the band is expected to be minimal, the composition (14.3 wt.% Sn, see Fig. 7) is close to C_α (13.5 wt.% Sn) and corresponds fairly well to the composition measured in lamellae near the quenched interface (see Fig. 9). Therefore, the bands clearly form near the peritectic temperature T_p and then evolve in thickness and composition due to the subsequent peritectic transformation.

value reported in the ASM Cu–Sn phase diagram (see Fig. 3) is 15.8 wt.% Sn at the eutectoid temperature (520 °C). Therefore, the bands which formed during solidification have evolved in order to maintain near-equilibrium conditions during the subsequent peritectic transformation.

During band formation, the composition at the growing interface is expected to increase as the α-phase grows whereas it must decrease once the β-phase has nucleated (see the mechanism detailed in Section 2, Fig. 1). This explains partially the right portion of the U-shape of the composition measured in the α-phase. However, it should be noted that during the peritectic transformation the composition $C_\alpha^{*\beta}$ at the α–β interfaces must increase from about 13.5 wt.% Sn to 15.8 wt.% Sn (see Fig. 3). Due to the slope of the α–β solvus, this means that the β-phase partially shrinks in order to provide the solute increase in the α-phase, i.e. the β-bands were thicker just after solidification. As a consequence, the U-shape composition profile also partially results from the peritectic transformation, thus explaining the left portion of the U-shape.

The composition of α-bands is not uniform because the Fourier number associated with their thickness is still fairly small. Indeed, the thickness d of these bands is typically 150 μm and the time t_d available for solid-state diffusion is equal to $\Delta T/(G_l V_p)$, where $G_l = 20$ K mm^{-1}, $V_p = 0.5$ μm s^{-1} and ΔT is the temperature difference from T_p to 500 °C. This gives $t_d \approx 3 \cdot 10^4$ s. For the Cu–Sn peritectic system, Oikawa and Hosoi [36] showed that the diffusion coefficient D_s in the α-phase is approximated by the following equation[2]:

Returning to the growth mechanism of these bands, the EBSD measurements in Fig. 6(B) show that α- and β-bands overlay each other rather than renucleate ahead of each other. This mechanism, which is of course not possible in two dimensions, is an extension of the island formation to three dimensions. It is schematically illustrated in Fig. 8 for an overlay of the primary phase by a new β-layer. Neglecting curvature and kinetic undercooling, the triple junction follows the peritectic temperature. In two dimensions, if the β-phase does not entirely cover the α-phase, β-islands are formed in an α-matrix. In three dimensions, the β-phase can apparently fully cover the primary phase in a metallographic section, but the α-phase might still regrow over it from a region not in the plane of Fig. 8(A).

This so-called partial banding or overlay mechanism has been observed experimentally in both sample geometries (4/6 mm tube and 3 mm diameter cylinder), and notably in the 3 mm diameter cylinder of a Cu–20 wt.% Sn alloy directionally solidified at 0.5 μm s^{-1} (see Fig. 6).

Looking at the EBSD false color reconstructed microstructure of Fig. 6(B), it also appears that renucleation of the α-phase ahead of the β-phase is possible. Indeed, a few isolated α-regions colored in light blue, light purple and yellow are visible in the upper part of the sample. Renucleation of the β-phase can also occur occasionally. Indeed, the β-phase could be indexed by EBSD in a few regions of Fig. 6(B) and at least two solid grains were revealed ahead of the large α + β lamellar structure. This renucleation mechanism of the primary and peritectic phases has already been described by Trivedi in a purely diffusive growth regime [4].

5.2. Formation of α + β lamellar structures

As can be seen in Fig. 6(B), the band structure leads to α + β lamellae with the same crystallographic orientation just above the line P1. Let us consider a mechanism

---

[2] Even if Eq. (2) is valid for temperatures between 727 and 827 °C, it has been extended in this work for lower temperatures.
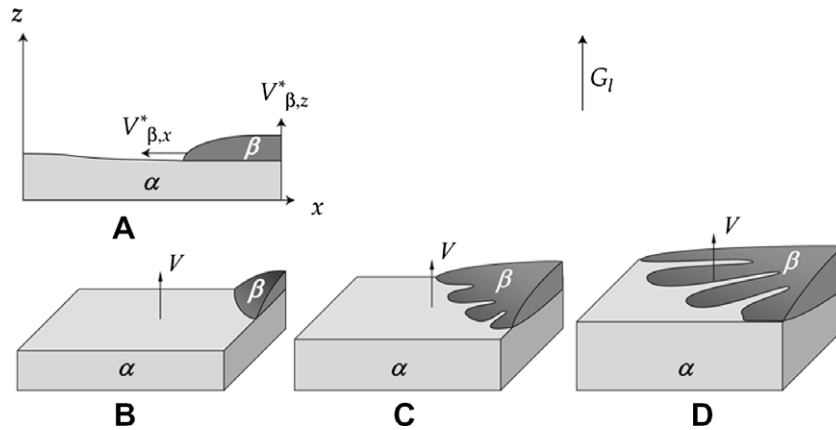
Fig. 8. Illustration of the β-phase nucleating and growing at some point on an advancing α–liquid interface, on a 2-D section in (A) and on a 3-D section in (B). (C) The lateral growth of the β-phase can be unstable, thus leading to the formation of cells. (D) The α-phase continues to grow in the thermal gradient direction in-between these β-cells, and an alternate sequence of α- and β-phases is therefore initiated. Reprinted from Dantzig and Rappaz [28].

naturally leading to the formation of lamellae from bands. As illustrated schematically in three dimensions in Fig. 8(B–D), the β-layer spreads over the α-phase in all directions (3-D growth), as already explained. Accordingly, the velocity normal to the β-layer is neither uniform nor constant: the corresponding lateral velocity $V^*_{\beta,x}$ is much larger than the velocity parallel to the growing direction $V^*_{\beta,z}$ (which is not necessarily equal to V_p under non-steady state conditions). As it spreads laterally very fast in the most undercooled region, the β–liquid interface can destabilize to form cells when 3-D growth is considered (see Fig. 8(C)). Since the α-phase is still growing in-between the spaces left by the β-cells, an alternate sequence of the primary and peritectic phases is formed and a "cooperative" growth is thus initiated between the α- and β-phases, leading to the formation of α + β lamellar structures. A similar situation can occur during the lateral propagation of an α-layer over a β–liquid interface. This mechanism is similar to that observed by Akamatsu et al. [37] on organic eutectic alloys at the onset of coupled growth.

Let us stress that lamellar structures have been observed in the 3 mm diameter cylinder for the hypoperitectic compositions studied in the present work (18.7 wt.% Sn, 20 wt.% Sn, 21 wt.% Sn and 21.3 wt.% Sn), while they were observed in the 4/6 mm tube exclusively for $C_0 = 21$ wt.% Sn and $C_0 = 21.3$ wt.% Sn (at $V_p = 0.5$, 0.58 μm s^{-1}). Natural convection plays a dominant role in the formation of α + β lamellar structures [38,39]: in the 4/6 mm tube, 3-D macrosegregation modeling revealed a nearly helical convection pattern in the liquid phase [34]. Between each convection cell, the fluid flow was mostly oriented parallel to the solid–liquid interface. As a consequence, the lateral propagation of the β-cells was surely affected by these convective motions. Similar arguments can be used for the formation of the lamellar structures in the 3 mm diameter cylinder, even if the fluid dynamics is expected to be more complex.

In Fig. 9, an α + β lamellar structure stable over a solidification distance of about 6 mm is shown. This structure has been observed in the 4/6 mm tube of a Cu–21 wt.%

Sn alloy directionally solidified at 0.58 μm s^{-1}. It took its origin again from α- and β-bands, as can be seen in Fig. 9(A). As solidification proceeds, the volume fraction of the α-phase seems to decrease (see Table 2). Then, at some point prior to the quench, the α-lamellae are overgrown by the β-phase, which grows further with a planar front morphology. At the time of the quench, the β planar front was positioned at 780 ± 5 °C (interface visible on the extreme right of Fig. 9(A)). Interestingly, the lamellar structure seems to alternate with a sequence of α-bands and islands. Again, EBSD analyses revealed that, rather than being discontinuous, the whole structure consists of two continuous α-solid grains (in blue and yellow; see Fig. 9(C)). This supports the overlay or partial banding mechanism and the instability of the band formation leading to lamellar structures.

An accurate determination of the average lamellar spacing $\bar{\lambda}$ is particularly difficult to achieve: on the one hand, all experimental observations showed that $\bar{\lambda}$ increases along the solidification direction as a result of termination mechanisms leading finally to the disappearance of α-lamellae. On the other hand, as will be shown hereafter, various arrangements for the α + β lamellar structure were observed in 2-D cross-sections: straight α- and β-lamellae, labyrinth-like microstructures and random arrangement of rods of one phase in the matrix of the other.

Unfortunately, α + β lamellar structures could not be observed in contact with the liquid phase at the time of the quench. In order to nevertheless estimate the operating temperature $T^*(x)$ and composition of the lamellar growth front, the compositions were measured across the lamellae at various positions (profiles P1, P2 and P3 in Fig. 9(A)). For both sample geometries, it was found that:

(1) For positions close to the quenched interface, the composition is almost uniform in both solid phases, in contrast to the profiles measured in the solidification direction over bands (see Fig. 7). It is periodic and fairly stable in each phase, thus indicating that
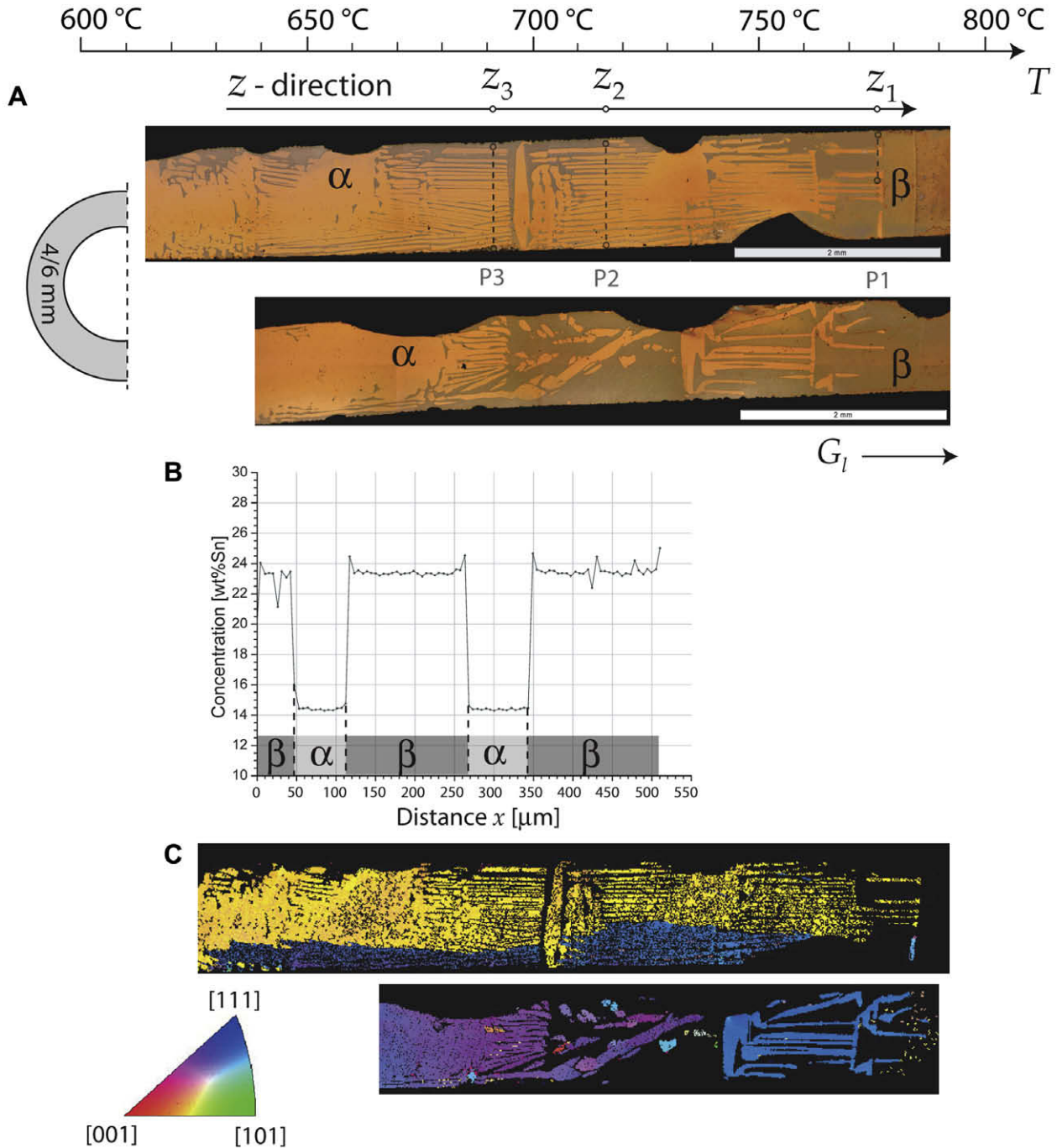
Fig. 9. (A) Lamellar structure observed during a DS experiment in a Cu–21 wt.% Sn sample (4/6 mm tube, $V_p = 0.58 \, \mu m \, s^{-1}$, $G_l = 20$ K mm^{-1}). The positions of the composition profiles P1, P2 and P3 are also indicated (α-phase = light brown, β-phase = dark brown). (B) Measured composition profile P1. (C) EBSD analyses in the inverse pole figure representation ([0 0 1] direction parallel to the z-direction).

Table 2
Average compositions in the α- and β-phases across the α + β lamellar structure (profiles P1–P3 in Fig. 9)

Profile No.	Average composition (wt.% Sn)	$\bar{C}_\alpha$ (wt.% Sn)	$\bar{C}_\beta$ (wt.% Sn)	g_α
P1	19.7	14.5	23.5	0.43
P2	18.5	15.5	24.9	0.69
P3	19.2	15.9	25.2	0.64

The volume fraction g_α of the α-solid phase is also indicated.

the α + β lamellar structures result from some kind of cooperative growth between the primary and peritectic phases. It should be noted that the small peaks in composition measured in the β-lamellae close to the α–β interfaces correspond to the nucleation of a small tin-rich phase during quenching.

(2) As one moves away from the quench interface, the compositions measured in the α- and β-lamellae steadily increases (see Table 2). Note that the composi-
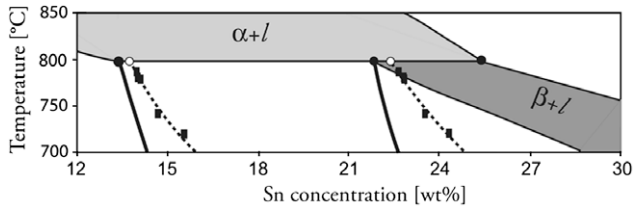
Fig. 10. The compositions and temperatures measured over lamellar structures for positions distant from the quenched interface ($F_o \gg 1$) are drawn on the Cu–Sn phase diagram (dark squares). Thick black lines correspond to solvus lines defined by the ASM phase diagram, while the filled circles indicate the equilibrium concentrations defined in Section 3. Dashed lines correspond to approximated solvus lines, whereas the corresponding equilibrium concentrations C_α and C_p are represented with open circles.

tion measured in the primary phase at P1, i.e. near the quench interface, is very close to the minimum composition measured in α-bands (see Fig. 7). Table 2 also lists the volume fraction of the α-phase, g_α, measured in this 2-D longitudinal section along the profiles P1–P3. As for the bands, the observed evolution of the composition along α- and β-lamellae is a result of peritectic transformation and solid-state diffusion. However, as the local compositions are measured for positions closer to the peritectic temperature, i.e. for positions corresponding to temperatures between 700 and 800 °C at the time of the quench (see Fig. 9(A)), the composition in the solid phases did not evolve as much as in the bands observed below the eutectoid temperature (see Figs. 6 and 7). Additionally, unlike bands, the composition in each lamella does not exhibit an initial solute inhomogeneity during solidification. The local compositions measured across lamellar structures at positions distant from the quenched interface (including profiles P2 and P3 of Fig. 9, but not exclusively) have been drawn on the Cu–Sn phase diagram at the corresponding measured temperatures. Assuming

that the α–β interfaces are at equilibrium, the measured compositions should lie on the corresponding solvus lines. As can be seen in Fig. 10, the obtained solvus lines and the extrapolated equilibrium compositions C_α and C_p at T_p differ from the Cu–Sn phase diagram defined in Section 3. However, substantial differences also exist between the various phase diagrams reported in the literature [32].

All lamellar structures ended by the termination of α-lamellae and the subsequent growth of a β-planar front. Quite interestingly, the α-lamellae observed in the 4/6 mm tube exhibited in all cases a "hammer-like" morphology before being overgrown by the peritectic phase, as can be seen in Fig. 11. Backscattered electron analyses revealed the presence of small precipitates in the β-phase between each hammer-like morphology, which nucleated probably during quenching but due to an inhomogeneity of composition induced during growth. Indeed, these precipitates are regularly arranged in semi-circles, possibly as a result of the composition field existing during the cooperative growth between α- and β-lamellae. Additionally, the rather polygonal interfaces shown in Fig. 11 tend to indicate that a partial peritectic transformation occurred after solidification of the lamellar structure. However, the solidification mechanisms leading to this "hammer-like" morphology remain to be understood. In the 3 mm diameter cylinder, no hammer-like morphology was observed at the end of α-lamellae. Indeed, EBSD analyses revealed that some of the isolated α-regions in a β-matrix have the same crystallographic orientation as the lamellar structure and resulted therefore from 3-D branching mechanisms. Accordingly, natural convection and the associated solute enrichment are assumed to be responsible for the destabilization of lamellar structures and the subsequent end of α-lamellae.

In order to observe the dynamic evolution of the geometrical arrangements of α- and β-phases in the lamellar structures, transverse cuts were also prepared. Fig. 12
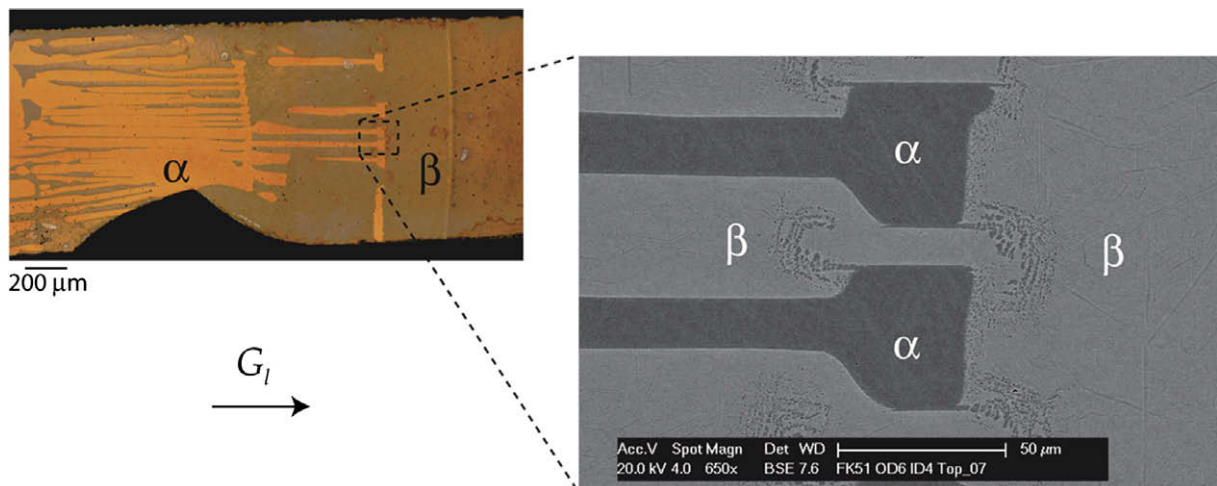

Fig. 11. The hammer-like morphology of α-lamellae revealed at the end of a lamellar structure observed in the 4/6 mm tube of a Cu–21 wt.% Sn sample directionally solidified at 0.58 μm s^{-1} ($G_l = 20$ K mm^{-1}).
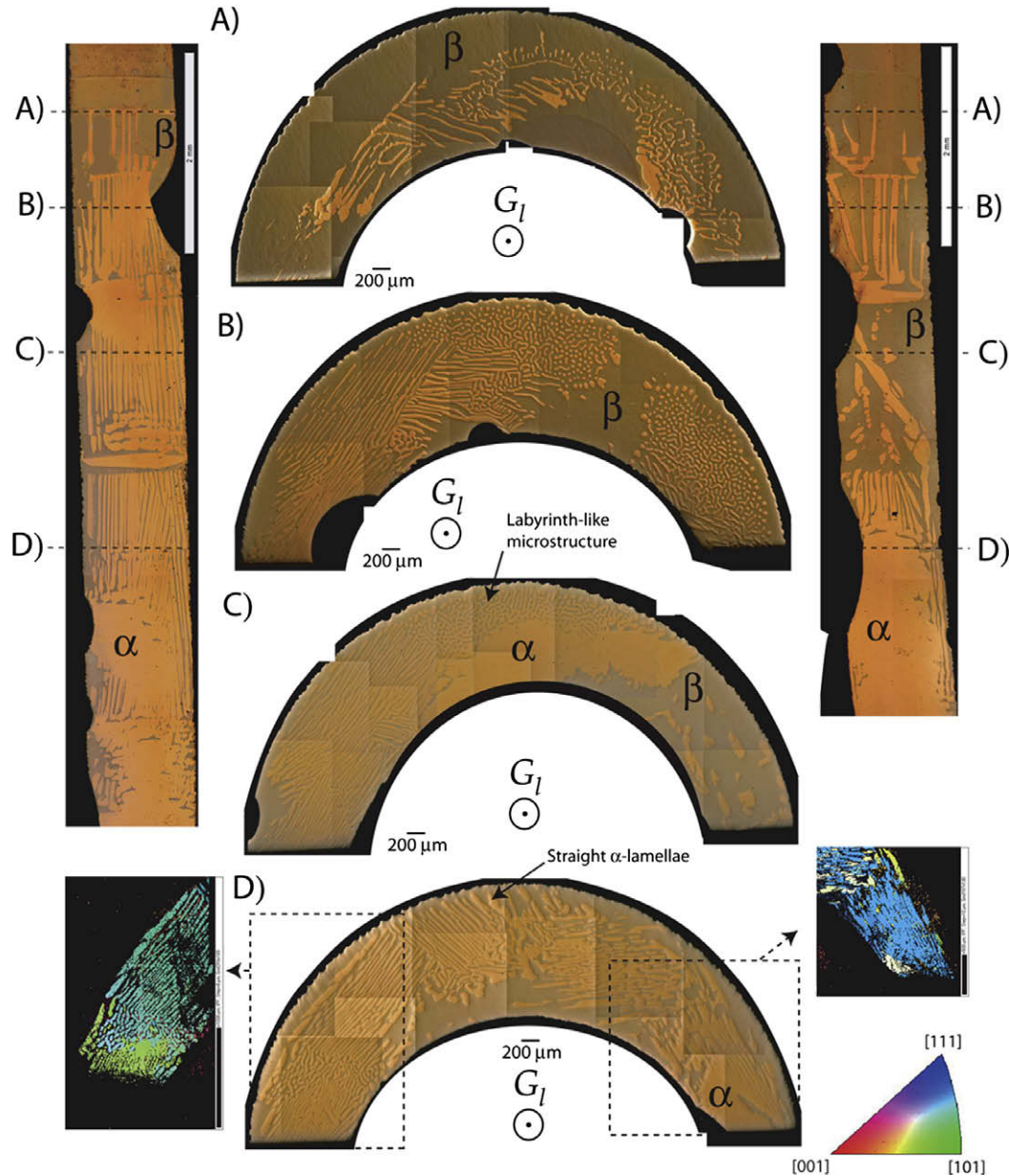
Fig. 12. Cross-sections of the $\alpha + \beta$ lamellar structure observed in the 4/6 mm tube of a Cu–21 wt.% Sn sample directionally solidified at 0.58 μm s^{-1} (G_l = 20 K mm^{-1}, the position of each cross-section is represented by a dashed curve, α-phase = light brown, β-phase = dark brown). EBSD analyses in the inverse pole figure representation show two portions of the cross-section (D) ([0 0 1] direction parallel to the z-direction).

presents four successive cross-sections of the lamellar structure observed in the 4/6 mm tube of the Cu–21 wt.% Sn sample directionally solidified at $V_p = 0.58$ μm s^{-1} (see Fig. 9). As can be seen, various arrangements are revealed, even in the same cross-section: straight α- and β-lamellae, labyrinth-like microstructures, disordered arrays of rods of one phase in the matrix of the other phase and uniform regions of β. As solidification proceeds, the volume fraction g_α of the primary phase decreases in agreement with the expected macrosegregation. At the same time, straight α-lamellae (Fig. 12(D)) destabilize progressively to form a labyrinth-like microstructure (Fig. 12(C) to (A)): first, this microstructure was composed of disordered arrays of β-rods and small sinuous β-lamellae surrounded by continu-

ous α-lamellae (Fig. 12(C)). Then, for lower volume fractions g_α, the lamellae of the α-phase fragmented in turn into disordered arrays of rods and small sinuous α-lamellae (Fig. 12(B) and (A)). In the cross-section (D), various orientations of straight lamellae are observed. EBSD analyses showed that the straight α-lamellae composing each orientation originated from a single solid grain. Additionally, these analyses revealed that several α-solid grains are present in the overall cross-section, i.e. multiple nucleation events during the partial banding mechanism preceding the cooperative growth between the α- and β-phases. The similarity between the above-mentioned dynamic evolution of α- and β-lamellae and 3-D multi-phase field modeling of eutectic-growth [40] is quite remarkable.
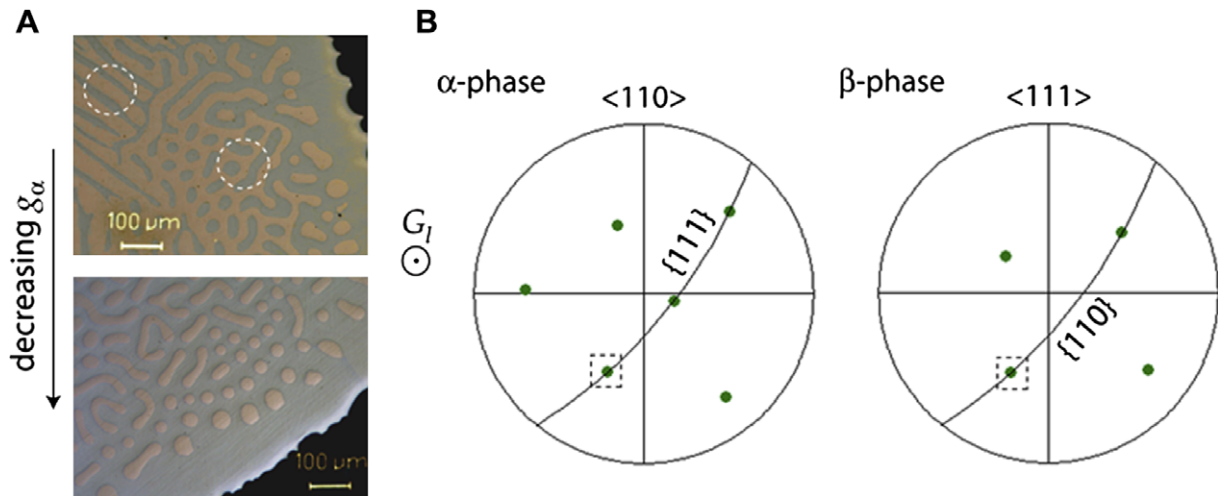
Fig. 13. Orientation relationship between the α- and β-phases in the lamellar structure (the same relationship observed in the straight lamellae and in the labyrinth-like microstructure). (A) Illustration of the position of the diffraction analyses over the cross-section. (B) Pole figures: for the fcc α-phase, the pole figures of ⟨1 1 0⟩ directions with a relative {1 1 1} plane are represented. On the other hand, for the bcc β-phase, the pole figures of ⟨1 1 1⟩ directions with a {1 1 0} plane are shown. As can be seen, the dashed squares emphasize the exact orientation relationship between the primary and peritectic phases in the lamellar structures. Indeed, this coherency relationship corresponds to the Kurdjumov–Sachs relationship.

In order to determine whether a loss of coherency relationship between the primary and peritectic phases occurred during the observed transition from the straight lamellae to the labyrinth-like microstructure, diffraction analyses were performed in $\alpha + \beta$ lamellar structures on transverse cuts where the peritectic phase did not decompose in the solid state. Such analyses have been made in the cross-section (D) of Fig. 12 over the straight lamellae and labyrinth-like microstructures. The same orientation relationship was observed for both microstructures, as can be seen in Fig. 13: the {1 1 1} plane of the fcc α-phase coincided with the {1 1 0} plane of the bcc β-phase with the so-called Kurdjumov–Sachs relationship, i.e. {1 1 1}$_\alpha$//{1 1 0}$_\beta$, ⟨1 1 0⟩$_\alpha$⟨1 1 1⟩$_\beta$.

Even if a crystallographic relationship exists between the primary and peritectic phase, it is essential to note that α–β interfaces are not necessarily coherent, as shown for regular eutectic structures, i.e. α–β interfaces are not exactly parallel to the planes of coherency. Consequently, the transition between the different geometrical arrangements in the lamellar structures result from growth competition mechanisms and instabilities between phases originated from the same nuclei.

6. Conclusions

An essential outcome of the present paper is that $\alpha + \beta$ bands and lamellar structures have been observed at low growth rates in both geometries of the Cu–Sn samples. Indeed, up to now, such morphologies have been observed only in peritectic systems for which the solidification interval of the primary phase is less than 10 °C. It has been shown that bands can occur from a 3-D overlay mechanism and not necessarily from a sequence of nucleation events. EBSD and microscopy analyses have shown that a cooper-

ative growth can be initiated between the α- and β-phases as in eutectic alloys by an unstable lateral propagation of one phase over the other. As a consequence, in contrast with previous investigations in Fe–Ni peritectic alloys [7,10,11], the island growth is not the sole initiation mode responsible for the formation of lamellar structures. Unfortunately, the $\alpha + \beta$ lamellar structures could not be observed in contact with the liquid phase at the time of the quench. The local compositions measured in the bands and lamellae indicate that the peritectic transformation affects the compositions and the fractions of solid phases. Considering the uncertainties of the Cu–Sn phase diagram and the composition evolution, it is clearly impossible to determine whether the growth front of $\alpha + \beta$ lamellar structures was isothermal or non-isothermal, and even more delicate, above or below T_p. In order to solve this issue, it is necessary to: (i) have a lamellar structure in contact with the liquid phase at the time of the quench; and (ii) reassess the phase diagram accurately. In this respect, the lamellar structures observed in the present work offer a unique way of determining the solvus lines for the primary and peritectic phases, up to the peritectic temperature.

Various geometrical arrangements for the lamellar structures were revealed on transverse cuts: straight α- and β-lamellae, labyrinth-like microstructures, disordered arrays of rods of one phase in the matrix of the other phase and uniform regions of β-phase. The dynamic evolution of lamellar structures was attributed to growth competition mechanisms and instabilities between phases originated from the same nuclei. Finally, a Kurdjumov–Sachs relationship was observed between the primary and peritectic phases on both the straight lamellae and the labyrinth-like microstructure.

All lamellar structures ended by the termination of α-lamellae and the subsequent growth of a β planar front.

The α-lamellae observed in the 4/6 mm tube exhibited in all cases a "hammer-like" morphology before being overgrown by the peritectic phase. Careful investigation of this morphology revealed that it resulted effectively from growth competition mechanisms, which are probably similar to those involved in the formation of islands. Convection still plays an important role and further measurements should be made in smaller capillaries or in a microgravity environment.

Acknowledgements

References

[1] Kerr HW, Kurz W. Int Metal Rev 1996;41:129–64.
[2] Boettinger WJ, Coriell SR, Greer AL, Karma A, Kurz W, Rappaz M, et al. Acta Mater 2000;48:43–70.
[3] Boettinger WJ. Metall Mater Trans 1974;5:2023–31.
[4] Trivedi R. Metall Mater Trans 1995;26A:1583–90.
[5] R. Trivedi, A. Karma, T.S. Lo, J.S. Park and M. Plapp. In: Solidification Microstructures, Proceedings of the 2nd Workshop, Zermatt, 1998.
[6] Tokieda K, Yasuda H, Ohnaka I. Mater Sci Eng 1999;A:238–45.
[7] Dobler S. Ecole Polytechnique Fédérale de Lausanne 2001:2409. These.
[8] Trivedi R, Park JS. J Crystal Growth 2002;235:572–88.
[9] Lo TS, Dobler S, Plapp M, Karma A, Kurz W. Acta Mater 2003;51:599–611.
[10] S. Dobler and W. Kurz, Z.Metallkd.;95: 592-595.
[11] Dobler S, Lo TS, Plapp M, Karma A, Kurz W. Acta Mater 2004;52:2795–808.
[12] Hunziker O, Vandyoussefi M, Kurz W. Acta Mater. 1998;46:6325–36.
[13] Mazumder P, Trivedi R, Karma A. Metall Mater Trans 2000;31A:1233–46.
[14] Park JS, Trivedi R. J Crystal Growth 1998;187:511–5.
[15] Chalmers B. Physical Metallurgy. New York: Wiley; 1959.
[16] Livingston JD. Mater Sci Eng 1971;7:61–70.
[17] Flemings MC. Solidification Processing. New York: McGraw-Hill; 1974.
[18] Lee JH, Verhoeven JD. J Crystal Growth 1994;144:353–66.
[19] Vandyoussefi M, Kerr HW, Kurz W. Acta Mater 2000;48:2297–306.
[20] Trivedi R, Miyahara H, Mazumder P, Simsek E, Tewari SN. J Crystal Growth 2001;222:365–79.
[21] Arai Y, Emi T, Fredriksson H, Shibata H. Metall Mater Trans 2005;36A:3065–74.
[22] McDonald NJ, Sridhar S. Metall Mater Trans 2003;34A:1931–40.
[23] Shibata H, Arai Y, Suzuki M, Emi T. Metall Mater Trans 2000;31B:981–91.
[24] Tiaden J. J Crystal Growth 1999;198/199:1275–80.
[25] Tiaden J, Nestler B, Diepers HJ, Steinbach I. Phys D 1998;115:73–86.
[26] Trivedi R. Scripta Mater 2005;53:47–52.
[27] Lo TS, Karma A, Plapp M. Phys Rev E 2001;63:31504.
[28] Dantzig J, Rappaz M. Solidification. EPFL Press; 2008.
[29] Pearson WB. A Handbook of Lattice Spacings and Structure of Metals and Alloys. New York: Pergamon Press; 1967.
[30] Cortie MB, Mavrocordatos CE. Metall Mater Trans 1991;22A:11–8.
[31] Liu XJ, Wang CP, Ohnuma I, Kainuma R, Ishida K. Metall Mater Trans 2004;35A:1641–53.
[32] Kohler F, Campanella T, Nakanishi S, Rappaz M. Acta Mater 2008;56(7):1519–28.
[33] American Society for Metals: Metals Handbook, Metallography, Structures and Phase Diagrams, 8th edn, Metals Park, OH, ASM, 1973.
[34] Kohler F. Ecole Polytechnique Fédérale de Lausanne 2008:4037. These.
[35] Hofmann U, Bögel A, Hölzl H, Kuhn H-A. Prakt Metallogr 2006;42(7):339–64.
[36] Oikawa H, Hosoi A. Scripta Metall 1975;9:823–8.
[37] Akamatsu S, Moulinet S, Faivre G. Metall Mater Trans 2001;32A:2039–48.
[38] Junze J, Kobayashi KF, Shingu PH. Metall Trans 1984;15:307–12.
[39] Lee JH, Liu S, Trivedi R. Metall Mater Trans 2005;36:3111–25.
[40] Plapp M. J Crystal Growth 2007;303:49–57.